



# Removing interlopers from intensity mapping probes of primordial non-Gaussianity

Chang Chen<sup>1★</sup> and Anthony R. Pullen<sup>1,2★</sup>

<sup>1</sup>Center for Cosmology and Particle Physics, Department of Physics, New York University, 726 Broadway, New York, NY 10003, USA

<sup>2</sup>Center for Computational Astrophysics, Flatiron Institute, New York, NY 10010, USA

Accepted 2022 February 24. Received 2022 February 15; in original form 2021 October 28

## ABSTRACT

Line intensity mapping (LIM) has the potential to produce highly precise measurements of scale-dependence bias from primordial non-Gaussianity (PNG) due to its ability to map much larger volumes than are available from galaxy surveys. However, LIM experiences contamination from foreground emission, including interloping emission lines from other redshifts that alter the power spectra of the maps at these scales, potentially biasing measurements of  $f_{\text{NL}}$ . Here, we model the effect of line interlopers on upcoming LIM probes of PNG from inflation. As an example, we consider the [C II] line at target redshift  $z_t = 3.6$  to probe PNG, with the important systematic concern being foreground contamination from CO lines residing at redshifts different from the target redshift. We find interloper lines can lead to a significant bias if we neglect the interlopers in the parameter estimation. Including the interlopers in the parameter estimation would cause an increase in errors for our PNG constraints, leading to a false positive for non-standard inflation models. We model how well the cross-correlation technique could reduce this interloper contamination using [C II] and CO(4–3) at the same redshift and find the uncertainty of  $f_{\text{NL}}$  reduces by factors of 2 and 6 for local and orthogonal shape PNG, respectively, and by a factor of 5 for local shape if we consider seven interloper lines. This shows that when jointly fitting the auto- and cross-spectrum in the presence of interlopers, the errors are comparable to those from fitting without interlopers, almost eliminating the effect of interlopers when measuring non-Gaussianity.

**Key words:** diffuse radiation – inflation – large-scale structure of Universe.

## 1 INTRODUCTION

Inflation theory has been enormously successful in explaining the origin of large-scale structure (LSS) in the universe (Guth 1981; Linde 1987). The simplest inflation model predicts almost scale-invariant, adiabatic and Gaussian perturbations. Primordial non-Gaussianity (PNG) of the local shape is parametrized by  $f_{\text{NL}}^{\text{loc}}$  (Komatsu & Spergel 2001; Gangui et al. 1994) as

$$\Phi = \phi + f_{\text{NL}}^{\text{loc}} \phi^2, \quad (1)$$

where  $\phi$  is the Gaussian primordial potential. The parameter  $f_{\text{NL}}$  for the standard single-field inflation model is very small of order  $10^{-2}$  (Maldacena 2003), while  $f_{\text{NL}}^{\text{loc}}$  for more general models, e.g. multi-field inflation (Linde & Mukhanov 1997; Lyth, Ungarelli & Wands 2003), is much higher, even up to  $f_{\text{NL}} \sim \mathcal{O}(1)$ . In addition, the orthogonal shape PNG, which can be produced by models with higher derivative interactions and Galilean inflation (Senatore, Smith & Zaldarriaga 2010), is parametrized by  $f_{\text{NL}}^{\text{orth}}$ . Therefore, probing  $f_{\text{NL}}$  can serve as a strong discriminant among cosmological models.

Currently, the best constraints on  $f_{\text{NL}}$  are from CMB bispectra measurements from Planck satellite, given as  $f_{\text{NL}}^{\text{loc}} = -0.9 \pm 5.1$  and  $f_{\text{NL}}^{\text{orth}} = -38 \pm 24$  (Planck Collaboration IX 2019). Complimentary, LSS surveys such as BOSS (Alam et al. 2017), DES (Abbott et al.

2018), and EUCLID (Amendola et al. 2018) could probe  $f_{\text{NL}}$  scale-dependent bias on large scales (Matarrese & Verde 2008; Afshordi & Tolley 2008) and are promising to achieve higher precision than CMB data. As of now, current constraints on  $f_{\text{NL}}^{\text{loc}}$  from scale-dependent bias are not yet competitive with CMB constraints (Leistedt, Peiris & Roth 2014; Castorina et al. 2019; Dai & Xia 2020), with the most precise constraints still coming from quasars in Leistedt et al. (2014),  $-49 < f_{\text{NL}}^{\text{loc}} < 31$ . For PNG of the general shape, non-zero primordial bispectrum induces a scale-dependent correction to the bias (Dalal et al. 2008; Matarrese & Verde 2008; Afshordi & Tolley 2008; Desjacques, Jeong & Schmidt 2011), leaving a signature in the power spectrum on large scales.

Unlike galaxy surveys that probe individual tracers, line intensity mapping (LIM) measures cumulative intensity fluctuations from all luminous sources including faint ones unresolved in galaxy surveys. LIM experiments could have the potential to access over 80 per cent of the volume of the observable Universe (Kovetz et al. 2019). Therefore, it has the potential to further the study of LSS in the universe, especially of the Epoch of Reionization when sources with low-luminosity inaccessible to galaxy surveys reionized the universe (Robertson et al. 2015). The fine-structure line from ionized carbon ([C II]) (Gong et al. 2012; Silva et al. 2015), the brightest line for star-forming galaxies, makes it an ideal candidate for probing the line intensity power spectrum on large scales to improve constraints of PNG (Moradinezhad Dizgah & Keating 2019; Moradinezhad Dizgah, Keating & Fialkov 2019).

★ E-mail: [changchen@nyu.edu](mailto:changchen@nyu.edu) (CC); [anthony.pullen@nyu.edu](mailto:anthony.pullen@nyu.edu) (ARP)

An important systematic effect when considering intensity mapping is foreground interloper emission (Visbal & Loeb 2010; Lidz & Taylor 2016; Cheng et al. 2016) from lines residing at the same *observed* frequency as the target line. Interloper emission, in which different emission lines from galaxies with different epochs redshift to the same observed frequency, contaminates intensity maps and introduces extra correlations in the measured power spectrum that can bias parameter estimations. This deposits a distinct signature at large scales, where effects from non-Gaussianity reside due to the features in the power spectrum at these scales such as baryon acoustic oscillations and the peak corresponding to matter-radiation equality.

In our case, we consider a target line of [C II] emission with rest-frame frequency  $\nu_t = 1901$  GHz emitted from sources at redshift  $z_t$  contaminated by interloping rotational lines of carbon monoxide (CO ( $J \rightarrow J-1$ )) (Visbal & Loeb 2010) with rest-frame frequency  $\nu_i = 115 \times JGHz$  emitted from sources at redshifts  $z_i$  lower than target redshift  $z_t$ . Those CO lines can be confused as [C II] line if they reside at the same observed frequency  $\nu_{\text{obs}}$  as the target line, i.e.  $\nu_{\text{obs}} = \nu_t/(1+z_t) = \nu_i/(1+z_i)$ . These interloper CO lines can distort power-spectrum detections and contaminate the forecast for constraints on PNG. A recent paper (Gong, Chen & Cooray 2020) discusses the interloper contamination on constraints of cosmological and astrophysical parameters. Assuming the target redshift  $z_t$  in converting the observed frequencies and angles to their co-moving coordinates, the interloper lines will be mapped to the wrong longitudinal and transverse co-moving wavenumbers, causing an anisotropy of the interloper power-spectrum contribution (Visbal & Loeb 2010; Gong et al. 2014; Lidz & Taylor 2016).

In this paper, we adopt this approach, where we seek how best to reduce the contamination when measuring  $f_{\text{NL}}$  using power-spectrum measurements. In this work, we consider an LIM survey using a Planck-like telescope with a high-resolution spectrograph, similar to the instrument modelled in Moradinezhad Dizgah et al. (2019), to forecast measurement errors for  $f_{\text{NL}}$ . We find through a Fisher analysis that not only do interlopers significantly increase the error on  $f_{\text{NL}}$ , but that a properly modelled autopower spectrum analysis cannot reduce the error effectively. Specifically, we find that interlopers can bias the  $f_{\text{NL}}$  measurement, producing a false  $3\sigma$  detection of non-Gaussianity favouring non-standard inflation models.

Next, we consider cross-correlation to separate anisotropic interloper emission from the [C II] autopower spectrum. We model the cross-correlation between [C II] and CO(4–3) at the same redshift,  $z = 3.6$  in our case with a different frequency to avoid bias from interloper emission. We calculate autopower spectra and cross-power spectrum of [C II] and CO(4–3) maps and perform a Fisher analysis to forecast the errors. We find the interloper contamination for the PNG probing can be largely removed using this method, reducing the Fisher analysis error by factors of 2 and 5 for  $f_{\text{NL}}^{\text{loc}}$  and  $f_{\text{NL}}^{\text{orth}}$ , respectively, if we only consider 1 interloper line, and by a factor of 5 for  $f_{\text{NL}}^{\text{loc}}$  if we consider 7 interloper lines. For both cases, we find that including the cross power in the analysis removes most of this interloper bias, making the  $f_{\text{NL}}$  measurement rather insensitive to contamination from interlopers. However, we also find that the autopower spectra can still play a large role in regards to the precision of the  $f_{\text{NL}}$  measurement. Specifically, we find that for  $f_{\text{NL}}^{\text{loc}}$ , the precision comes solely from the cross-power spectrum, while for  $f_{\text{NL}}^{\text{ortho}}$  the precision comes roughly equally from the autopower and cross-power spectra.

The outline of the rest of the paper is as follows. In Section 2, we review the theoretical model of the line intensity power spectrum detection for PNG, and the interloper contamination for this detection. In Section 3, we describe the Fisher analysis and data bias approach.

In Section 4, we detail our fiducial survey and present the results for constraints on  $f_{\text{NL}}^{\text{loc}}$ . We further discuss the prospect for using cross-correlation with another emission line in Section 5. In Section 6, we forecast the constraints on the orthogonal shape PNG. We further consider different astrophysical models in Section 7. Based on our results, we draw our conclusions in Section 8. Throughout this paper, we adopt a flat cosmological model with  $H_0 = 67.74$ ,  $\Omega_m = 0.26$ ,  $\Omega_b = 0.049$ , and  $\sigma_8 = 0.816$ .

## 2 PNG LINE INTENSITY POWER-SPECTRUM DETECTION AND INTERLOPER CONTAMINATION

In this section, we review the formalism for the scale-dependent correction to clustering bias due to non-zero  $f_{\text{NL}}$ , present how this correction to bias would manifest itself in the line intensity power-spectrum detection, and highlight the interloper contamination of the power spectrum.

### 2.1 PNG review

Local shape PNG is produced by super-horizon non-linear evolution of primordial curvature perturbations. In the absence of PNG, on large scales the halo bias  $b_h$  is assumed to be constant. Local shape PNG, parametrized by  $f_{\text{NL}}^{\text{loc}}$ , leads to a scale-dependent correction to the linear halo bias (Dalal et al. 2008; Matarrese & Verde 2008; Afshordi & Tolley 2008):

$$b_h(M, z) \rightarrow b_h(M, z) + \Delta b_h^{\text{loc}}(M, k, z), \quad (2)$$

$$\Delta b_h^{\text{loc}}(M, k, z) = \frac{3 f_{\text{NL}}^{\text{loc}} \delta_c [b_h(M, z) - 1] \Omega_m H_0^2}{k^2 T(k) D(z)}, \quad (3)$$

where  $\delta_c = 1.686$  is the threshold of spherical collapse at  $z = 0$ ,  $T(k)$  is the matter linear transfer function  $T(k \rightarrow 0) = 1$ , and  $D(z)$  is the normalized linear growth factor [ $D(z = 0) = 1$ ]. On large scales, this  $k^{-2}$  scale-dependent correction has been used to constrain  $f_{\text{NL}}^{\text{loc}}$  from power-spectrum detections of LSS biased tracers due to its clean signal (Slosar et al. 2008; Leistedt et al. 2014; Ho et al. 2015). Alternatively, LIM can provide a more economical survey over larger volume to probe power spectrum on large scales.

Orthogonal shape PNG can be produced by models with higher derivative interactions and Galilean inflation (Senatore et al. 2010). Parametrized by  $f_{\text{NL}}^{\text{orth}}$ , on large scales, orthogonal shape PNG leads to a scale-dependent correction to the linear halo bias (Desjacques et al. 2011)

$$\Delta b_h^{\text{orth}}(k) = -6 f_{\text{NL}} \frac{\sigma_{\alpha s}^2}{\sigma_{0s}^2} \left[ (b_h - 1) \delta_c + 2 \left( \frac{\partial \ln \sigma_{\alpha s}}{\partial \ln \sigma_{0s}} - 1 \right) \right] \times k^{-2\alpha} \mathcal{M}_{R_s}(k, z)^{-1} \quad (4)$$

$\alpha = (n_s - 4)/6$ ,  $\mathcal{M}_{R_s}(k, z) = W_{R_s}(k) \mathcal{M}(k, z)$ , where  $\mathcal{M}(k, z) = \frac{2}{5} \frac{k^2 T(k) D(z)}{\Omega_m H_0^2}$ , and we choose the window function  $W_{R_s}(k)$  as the Fourier transform of a spherical top-hat filter with smoothing length  $R_s = (3M/4\pi\bar{\rho})^{1/3}$ ,

$$W_{R_s}(k) = \frac{3 [\sin(k R_s) - k R_s \cos(k R_s)]}{(k R_s)^3}. \quad (5)$$

The general spectrum moment is

$$\sigma_{\alpha s}^2 = \frac{1}{2\pi^2} \int_0^\infty dk k^{2(\alpha+1)} P_\Phi(k) \mathcal{M}_{R_s}(k, z)^{-1}. \quad (6)$$

## 2.2 Line intensity power spectrum

Here, we model the [C II] line intensity power spectrum to predict how well it could constrain PNG. The relation between the mean intensity of the emission line and the luminosity of [C II]-luminous galaxies in their host haloes (Visbal & Loeb 2010; Moradinezhad Dizgah & Keating 2019) at redshift  $z$  is expressed as

$$\langle I_{\text{CII}} \rangle(z) = \frac{c^2 p_{1,\sigma}}{2k_B v_{\text{obs}}^2} \int_{M_{\text{min}}}^{M_{\text{max}}} dM \frac{dn}{dM} \frac{L(M, z)}{4\pi D_L^2} \left( \frac{dl}{d\theta} \right)^2 \frac{dl}{dv}, \quad (7)$$

where  $M_{\text{min}}$  and  $M_{\text{max}}$  are the minimum and maximum mass of [C II]-emitting haloes,  $p_{n,\sigma}$  accounts for the increase in power due to scatter in the  $L_{[\text{CII}]}(M)$  relation and is given in Moradinezhad Dizgah & Keating (2019) as

$$p_{n,\sigma} = \int_{-\infty}^{+\infty} dx \frac{10^{nx}}{\sqrt{2\pi}\sigma_{\text{line}}} e^{-x^2/\sigma_{\text{line}}^2}, \quad (8)$$

where  $n = 1$  for  $\langle I_{\text{line}} \rangle$ , and  $n = 2$  for  $\langle P_{\text{shot}} \rangle$ ;  $\sigma_{\text{line}}$  is the single, aggregate scatter parameter, and is set to be 0.37.  $dn/dM$  is the halo mass function,  $L(M, z)$  is the luminosity of the [C II]-luminous galaxies from dark matter halo of mass  $M$  at redshift  $z$ , and  $D_L$  is the luminosity distance. We set  $M_{\text{min}} = 10^9 M_\odot$  and  $M_{\text{max}} = 10^{14.5} M_\odot$ . We use the Tinker halo mass function (Tinker et al. 2008).  $dl/d\theta$  and  $dl/dv$  convert comoving lengths  $l$  to frequency  $\nu$  and angular size  $\theta$ ,  $dl/d\theta = D_{A,\text{co}}(z)$ ,  $\frac{dl}{dv} = \frac{c(1+z)}{v_{\text{obs}} H(z)}$ , where  $D_{A,\text{co}}(z)$  is the comoving angular diameter distance (for a flat universe,  $D_{A,\text{co}}(z) = \chi(z)$ , where  $\chi(z)$  is the co-moving distance to redshift  $z$ ) and  $H(z)$  is the Hubble parameter at redshift  $z$ . For our fiducial model, we use the result of the  $m1$  model of Silva et al. (2015) to relate the [C II] luminosity to the average star formation rate  $\overline{\text{SFR}}(M, z)$  of Behroozi, Wechsler & Conroy (2013)

$$\log L_{\text{CII}} = 0.8475 \times \log \overline{\text{SFR}}(M, z) + 7.2203 \quad (9)$$

[CII] line bias is related to halo bias  $b_h(M, z)$  as (Moradinezhad Dizgah & Keating 2019)

$$b_{\text{line}}(z) = \frac{\int_{M_{\text{min}}}^{M_{\text{max}}} dM \frac{dn}{dM} b_h(M, z) L(M, z)}{\int_{M_{\text{min}}}^{M_{\text{max}}} dM \frac{dn}{dM} L(M, z)}. \quad (10)$$

We use halo bias  $b_h(M, z)$  of Tinker et al. (2010).

Setting  $z = 3.60$ , we get  $\langle I_{\text{CII}}(3.6) \rangle = 0.30 \mu\text{K}$  from (7) and  $b_{\text{line}}(3.6) = 3.47$  from equation (10).

The shot noise power spectrum is

$$P_{\text{shot}}(z) = \frac{c^4 p_{2,\sigma}}{4k_B^2 v_{\text{obs}}^4} \int_{M_{\text{min}}}^{M_{\text{max}}} dM \frac{dn}{dM} \left[ \frac{L(M, z)}{4\pi D_L^2} \left( \frac{dl}{d\theta} \right)^2 \frac{dl}{dv} \right]^2. \quad (11)$$

Including redshift space distortions, the line clustering power spectrum can be expressed as

$$P(k, \mu, z) = \langle I_{\text{CII}} \rangle(z)^2 b_{\text{line}}^2(z) P_0(k, z) \times [1 + \mu^2 \beta(k, z)]^2 \exp \left( -\frac{k^2 \mu^2 \sigma_v^2}{H^2(z)} \right). \quad (12)$$

The factor of  $[1 + \mu^2 \beta(k, z)]^2$  comes from the Kaiser effect (Kaiser 1987),  $\beta(k, z) = f/b_{\text{line}}(z)$ , where  $f$  is the logarithmic derivative of the growth factor,  $\mu = k_{\parallel}/k$  is the cosine of the angle between the  $k$  and the line of sight direction. The factor of  $\exp \left( -\frac{k^2 \mu^2 \sigma_v^2}{H^2(z)} \right)$  is from the finger-of-god effect (Jackson 1972) with the pairwise velocity dispersion approximated as  $\sigma_v^2 = (1+z)^2 \left[ \frac{\sigma_{\text{FOG}}^2(z)}{2} + c^2 \sigma_z^2 \right]$ , where  $\sigma_{\text{FOG}}(z) = \sigma_{\text{FOG},0} \sqrt{1+z}$ ,  $\sigma_z = 0.001(1+z)$ , and  $\sigma_{\text{FOG},0} = 250 \text{ km s}^{-1}$ . According to equations (10), (2), and (3) will manifest as a scale-dependent correction to the  $b_{\text{line}}$  and therefore to the line power spectrum (12).

## 2.3 Interloper contamination

Line emission of CO interloper line at redshift  $z_i$  confuses with target [C II] line by residing at the same observed frequency  $\nu_{\text{obs}}$  as the [C II] line. When we convert the observed frequency interval  $\Delta\nu_{\text{obs}}$  and angular separation  $\Delta\theta_{\text{obs}}$  in a data cube to co-moving coordinates to calculate the power spectrum, if we adopt the target line redshift  $z_t$ , we will end up with wrong wavenumbers (Lidz & Taylor 2016). The relation between the true wavenumbers  $k_{\parallel}$  and  $k_{\perp}$  and these apparent wavenumbers  $\tilde{k}_{\parallel}$  and  $\tilde{k}_{\perp}$ , calculated by wrongly adopting the  $z_t$  for coordinate conversion, is

$$\tilde{k}_{\parallel} = \frac{H(z_t)}{H(z_i)} \frac{1+z_i}{1+z_t} k_{\parallel} = \alpha_{\parallel} k_{\parallel}, \quad (13)$$

$$\tilde{k}_{\perp} = \frac{D_{A,\text{co}}(z_i)}{D_{A,\text{co}}(z_t)} k_{\perp} = \alpha_{\perp} k_{\perp}, \quad (14)$$

where  $\alpha_{\parallel}$  and  $\alpha_{\perp}$  are distortion factors caused by this incorrect redshift adoption. Therefore, for the multiple interloper line emission case with  $N$  interloper lines, the total power spectrum in the data cube is

$$P_{\text{tot}}(\tilde{k}_{\parallel}, \tilde{k}_{\perp}) = P_t(k_{\parallel}, k_{\perp}) + \sum_{j=1}^N \frac{1}{\alpha_{\parallel}(z_j) \alpha_{\perp}^2(z_j)} P_j \left( \frac{\tilde{k}_{\parallel}}{\alpha_{\parallel}}, \frac{\tilde{k}_{\perp}}{\alpha_{\perp}} \right), \quad (15)$$

where  $z_j$  is the redshift of the  $j$ th interloper line. In this paper, we consider up to 7 CO interloper lines, with  $J$  ranging from 4 to 10 in CO( $J \rightarrow J-1$ ) molecule transitioning between rotational states  $J$  and  $J-1$ . Ignoring the interloper power spectrum from the second term in equation (15) would lead to data bias to the parameter estimation.

For CO( $1 \rightarrow 0$ ), expressed in units of solar luminosity, the luminosity is

$$L_{\text{CO}(1-0)} = 4.9 \times 10^{-5} L'_{\text{CO}}. \quad (16)$$

Using the fit from (Carilli & Walter 2013), CO line luminosity  $L'_{\text{CO}}$ , which is expressed in units of  $\text{K km s}^{-1} \text{pc}^2$ , is related to the far-infrared luminosity  $L_{\text{IR}}$ , which is in the unit of  $L_\odot$  as

$$\log L_{\text{IR}} = 1.37 \times \log L'_{\text{CO}} - 1.74. \quad (17)$$

We use the base model of Li et al. (2016), where  $L_{\text{IR}}$  is related to the  $\overline{\text{SFR}}$  in units of  $M_\odot \text{yr}^{-1}$  via Kennicutt relation (Kennicutt 1998) using the results of Behroozi et al. (2013)

$$\overline{\text{SFR}}(M, z) = \delta_{\text{MF}} \times 10^{-10} L_{\text{IR}}. \quad (18)$$

We use  $\delta_{\text{MF}} = 1$  (Behroozi et al. 2013; Li et al. 2016).

Using equation (7), we get intensities for CO( $1 \rightarrow 0$ ) at different redshifts  $z_j$  that will interlope with the [C II] target line at  $z = 3.6$ , i.e.  $\frac{J \times 115 \text{ GHz}}{z_j + 1} = \frac{1901 \text{ GHz}}{3.6 + 1}$ . In order to construct a rough estimate of the interloper luminosities, we use the ratio between the luminosity of 7 CO interloper lines with  $J$  ranging from 4 to 10 and that for the CO( $1 \rightarrow 0$ ) (Visbal & Loeb 2010) to get the intensities for these 7 interlopers, we also calculate the line biases for these interloper lines according to equation (10); these values for interlopers are listed in Table 1.

According to the values in Table 1, we plot spherically averaged  $k^3 P(k)/(2\pi)^2$  of the [C II] line at  $z = 3.6$  and the 7 CO lines that interlope with it in Fig. 1. As in previous work (Lidz & Taylor 2016; Gong et al. 2012), we plot contours of constant power in the  $k_{\perp}-k_{\parallel}$  plane in Figs 2 and 3 to visualize the anisotropy of the sum of the seven interloper power spectrum. Fig. 2 characterizes the redshift space distortion in the target [C II] line power spectrum. The contours in Fig. 3 illustrate the anisotropy of the power spectrum summation



**Table 1.** Redshifts  $z_j$ , intensities  $\langle I \rangle$  (in units of  $\mu\text{K}$ ), and line biases  $b_{\text{line}}$  for the 7 interloper CO lines.

J	4	5	6	7	8	9	10
$z_j$	0.113	0.391	0.670	0.948	1.226	1.504	1.783
$\langle I \rangle$	0.07	0.08	0.10	0.06	0.04	0.03	0.02
$b_{\text{line}}$	0.6	0.8	1	1.2	1.3	1.4	1.6

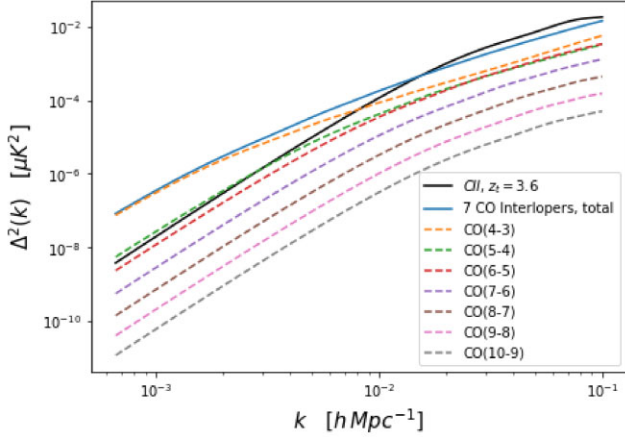


**Figure 1.** Spherically averaged  $k^3 P(k)/(2\pi^2)$ . The black solid line shows the [C II] line power spectrum at  $z = 3.6$ . The blue solid line shows the total interloper power spectrum from the 7 CO interloper lines. The 7 dashed lines show the interloper power spectrum for the 7 CO interloper lines, respectively.

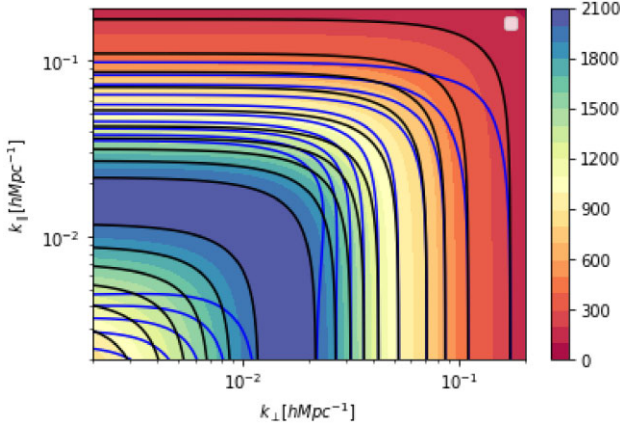


**Figure 2.** Contours of constant power in the  $k_{\perp}-k_{\parallel}$  plane for the target [C II] power spectrum at  $z_t = 3.6$ . The black contours neglect redshift space distortions, while the blue contours and colour-scale include them. The colourbar is in units of  $\mu\text{K}^2(\text{Mpc}/h)^3$ .

of the interloper CO lines from the coordinate mapping distortion, with the  $k_{\parallel}$  strongly elongated.

### 3 PARAMETER ESTIMATION FORMALISM

The first part of this section describes the Fisher matrix forecast methodology. In the second part, we derive the interloper bias to the measured power spectrum.

#### 3.1 Fisher matrix forecast

We use the Fisher matrix methodology to forecast how well a hypothetical [C II] survey will constrain  $f_{\text{NL}}$ . We first consider the

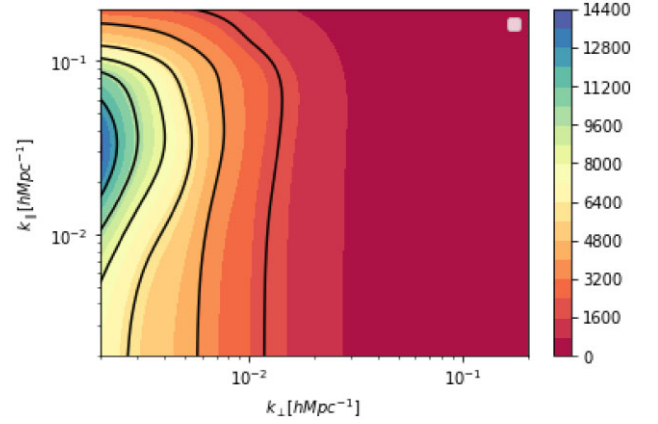


**Figure 3.** The contour with lowest power is at  $P(k) = 2 \times 10^3 \mu\text{K}^2(\text{Mpc}/h)^3$  and the contours increase inwards as  $\Delta P = 2 \times 10^3 \mu\text{K}^2(\text{Mpc}/h)^3$ . The black contours illustrate the anisotropy of the summation of the seven interloper line power spectrum including redshift space distortion and coordinate mapping distortion. The  $k_{\parallel}$  direction is strongly elongated.

simple case with only 1 CO interloper CO(4  $\rightarrow$  3). We consider a parameter space  $\mathbf{q}$ . Our forecast is conducted at  $z_t = 3.6$ .

We investigate whether the  $f_{\text{NL}}$  and [C II] target line, which is characterized by  $I_{\text{C II}}$  and  $b_{\text{C II}}$  can be forecasted precisely with the interloper contamination which is characterized by  $\langle I_{\text{CO}(4 \rightarrow 3)} \rangle$  and  $b_{\text{CO}(4 \rightarrow 3)}$  by calculating the Fisher matrix with component for the  $i$ th and  $j$ th of  $\mathbf{q}$

$$F_{ij} = \int_{-1}^1 d\mu \int_{k_{\min}}^{k_{\max}} \frac{k^2 dk}{8\pi^2} V_{\text{eff}}(k, \mu, z_t) \frac{\partial \ln P_{\text{tot}}(k, \mu, z_t)}{\partial q_i} \times \frac{\partial \ln P_{\text{tot}}(k, \mu, z_t)}{\partial q_j}, \quad (19)$$

where the total power spectrum including the [C II] and CO(4  $\rightarrow$  3) power is given as equation (15).  $V_{\text{eff}}$  is the effective volume of the redshift bin at  $z_t = 3.6$ ,  $V_{\text{eff}} = \left[ \frac{P_{\text{tot}}(k, \mu, z_t)}{P_{\text{tot}}(k, \mu, z_t) + P_{\text{shot}}(z_t) + P_N(k, \mu)} \right]^2 V_i$ ,  $P_{\text{shot}}(z_t)$  is given as equation (11),  $\tilde{P}_N(k, \mu)$  is the effective instrumental noise power spectrum given later as equation (28),  $V_i$  is the volume of the redshift bin between  $z_{\min}$  and  $z_{\max}$  with a fraction of the sky  $f_{\text{sky}}$ ; specifically,  $V_i = \frac{4\pi}{3} f_{\text{sky}} [\chi^3(z_{\max}) - \chi^3(z_{\min})]$ , where  $\chi(z)$  is the co-moving distance to redshift  $z$ .

#### 3.2 Parameter bias forecast

If we neglect the interlopers in the parameter estimation, the bias from interloper contamination in power-spectrum detection can be calculated using the formalism constructed in Pullen et al. (2016). The parameter bias is

$$\Delta \mathbf{q} = \mathbf{F}^{-1} \Delta \mathbf{D}, \quad (20)$$

where  $\mathbf{F}$  is the Fisher matrix with the parameter space of  $\mathbf{q}$ . The  $j$ th component of  $\Delta \mathbf{D}$  is given as

$$\Delta D_j = \int_{-1}^1 d\mu \int_{k_{\min}}^{k_{\max}} \frac{k^2 dk}{8\pi^2} V_{\text{eff}}(k, \mu, z_t) \frac{\Delta P_t(k, \mu, z_t)}{P_t} \times \frac{\partial \ln P_t(k, \mu, z_t)}{\partial q_j}, \quad (21)$$

where  $\Delta P_t(k, \mu, z_t)$  is the bias the interlopers contribute to the target power spectrum  $P_t(k, \mu, z_t)$ , i.e. the second term in equation (11).

## 4 FIDUCIAL SURVEY AND RESULTS

Having quantified the PNG contribution to the [C II] line power spectrum and its interloper contamination, we describe our hypothetical fiducial survey in the first part of this section, and present forecasts for using this to remove the CO interloper contributions from the [C II] local shape PNG power spectrum detection in the second part.

### 4.1 Fiducial survey description

As in Moradinezhad Dizgah & Keating (2019), we consider an Planck-like telescope having an aperture with dish length of  $D_{\text{ant}} = 1.5$  m. We assume a frequency range of 310–620 GHz, corresponding to a [C II] redshift range of  $z = 2.06$ – $5.13$ , and a frequency resolution  $\Delta\nu = 0.4$  GHz, aperture temperature  $T_{\text{aperture}} = 40$  K, and approximately  $N_{\text{det}} = 10^4$  detectors working for  $\tau_{\text{tot}} = 4 \times 10^4$  hr. We assume a survey sky coverage fraction  $f_{\text{sky}} = 0.34$ , which leads to an angular limit on the sky of  $\theta_{\text{max}} = \sqrt{\Omega_{\text{surv}}} = \sqrt{4\pi f_{\text{sky}}} = 118^\circ$ .

We include in our noise model photon noise from the CMB ( $T_B = 2.725$  K), galactic dust ( $T_B = 18$  K), and zodiacal dust ( $T_B = 240$  K) contributions. The emissivity of the dust is  $\varepsilon = \varepsilon_0(\nu/\nu_0)^\beta$ , where for galactic dust emission  $\varepsilon_0 = 2 \times 10^{-4}$ ,  $\nu_0 = 3$  THz,  $\beta = 2$ ; while for zodiacal dust emission  $\varepsilon_0 = 3 \times 10^{-7}$ ,  $\nu_0 = 2$  THz,  $\beta = 2$ . The radiation emitted at frequency  $\nu$  is

$$I_\nu = \varepsilon(\nu)B_\nu(T) = \varepsilon(\nu) \frac{2h\nu^3}{c^2} \frac{1}{e^{h\nu/k_B T_B} - 1}. \quad (22)$$

The Rayleigh–Jeans law yields

$$T_{\text{dust}} = \frac{\varepsilon(\nu)B_\nu(T)c^2}{2\nu^2 k_B} = \varepsilon(\nu)h\nu \frac{1}{k_B(e^{h\nu/k_B T_B} - 1)}. \quad (23)$$

From equation (23), we get that at the observed frequency for the [C II] line,  $T_{\text{galactic dust}} = 46 \mu\text{K}$  and  $T_{\text{zodiacal dust}} = 53 \mu\text{K}$ ; therefore, the systematic temperature is

$$T_{\text{sys}} = T_{\text{aperture}} + T_{\text{CMB}} + T_{\text{zodiacal dust}} + T_{\text{galactic dust}} = 42.725 \text{ K}. \quad (24)$$

The instrumental noise for each  $k$  mode is (Moradinezhad Dizgah et al. 2019)

$$P_N = \frac{T_{\text{sys}}^2}{\tau_{\text{tot}} N_{\text{det}}} \Omega_{\text{surv}} \left( \frac{dl}{d\theta} \right)^2 \frac{dl}{d\nu}. \quad (25)$$

The scale-independent correction to the clustering bias is relatively negligible at small scales, so we set  $k_{\text{max}} = 0.1h \text{ Mpc}^{-1}$ .

We consider the largest scales recoverable from foreground contamination. We model this with the parameter  $\eta_{\text{min}}$ , defined as the ratio of the observed frequency divided by the maximum bandwidth over which the frequency dependent response of the instrument is assumed to be smooth, as in Moradinezhad Dizgah & Keating (2019). We model the recoverable largest-scale perpendicular mode from foregrounds as  $k_{\perp, \text{min}} = 2\pi\eta_{\text{min}}[\nu_{\text{obs}} dl/d\nu]^{-1}$ . Setting  $\eta_{\text{min}} = 4.5$ , which is  $3\times$  the frequency-bandwidth ratio of the fiducial instrument, we have  $k_{\perp, \text{min}} = 0.0077 \text{ Mpc}^{-1}$ . The survey area sets the largest-scale perpendicular mode, given by  $k_{\perp, \text{min}} = 2\pi[2 \sin(\theta_{\text{max}}/2) \frac{dl}{d\theta}]^{-1} = 0.0005 \text{ Mpc}^{-1}$ . The smallest scale modes are generated by the spatial and spectral resolutions, respectively,  $k_{\perp, \text{max}} \approx 2\pi[\frac{c/\nu_{\text{obs}}}{D_{\text{ant}}} \frac{dl}{d\theta}]^{-1}$ ,  $k_{\parallel, \text{max}} \approx 2\pi[\delta\nu \frac{dl}{d\nu}]^{-1}$ . We introduce the attenuation of the signal due to foregrounds as in Moradinezhad Dizgah & Keating (2019)

$$\gamma_{\text{min}}(k_{\perp}, k_{\parallel}) = \left(1 - e^{-k_{\perp}^2/(k_{\perp, \text{min}}/2)^2}\right) \times \left(1 - e^{-k_{\parallel}^2/(k_{\parallel, \text{min}}/2)^2}\right), \quad (26)$$

**Table 2.** Fisher analysis results for  $f_{\text{NL}}^{\text{loc}}$ .

Interloper number	0	1	7
$\sigma(f_{\text{NL}}^{\text{loc}}$ for autospectrum)	1.32	1.64	4.04
$\sigma(f_{\text{NL}}^{\text{loc}}$ for cross-spectrum)	0.72	0.85	1.12
$\sigma(f_{\text{NL}}^{\text{loc}}$ for auto and cross-spectrum)	0.65	0.69	0.85

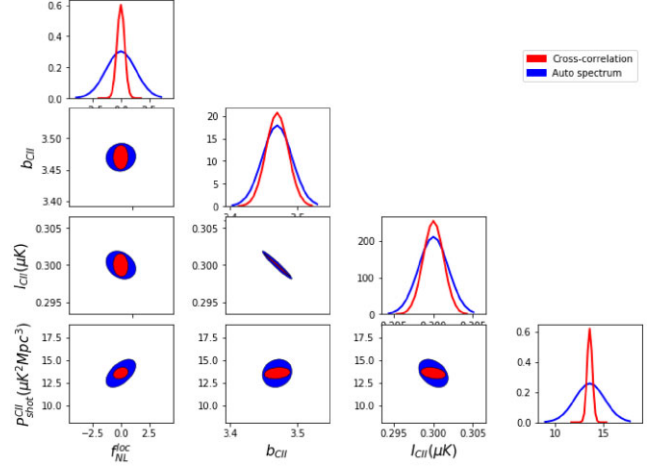


**Figure 4.**  $1-\sigma$  forecast of the constraint on  $f_{\text{NL}}^{\text{loc}}$  for the Fisher analysis without considering interlopers.

and due to finite spectral and angular resolution

$$\gamma_{\text{max}}(k_{\perp}, k_{\parallel}) = e^{-(k_{\perp}^2/k_{\perp, \text{max}}^2 + k_{\parallel}^2/k_{\parallel, \text{max}}^2)}, \quad (27)$$

writing the effective instrumental noise as

$$\tilde{P}_N(k, \mu, z) = P_N \gamma_{\text{max}}^{-1}(k, \mu) \gamma_{\text{min}}^{-1}(k, \mu). \quad (28)$$

### 4.2 Forecast results

In this section, we forecast the local shape  $f_{\text{NL}}$  measured from only the autopower spectrum. The Fisher analysis results for this section are listed in Table 2.

In the first scenario, we assume there is no interloper contamination. The parameter space includes four parameters  $\mathbf{q} = \{f_{\text{NL}}^{\text{loc}}, \langle I_{\text{CII}} \rangle, b_{\text{CII}}, P_{\text{shot}}^{\text{CII}}\}$ . We set the fiducial value of the parameters as  $f_{\text{NL}}^{\text{loc}} = 0$ ,  $\langle I_{\text{CII}} \rangle = 0.30 \mu\text{K}$ ,  $b_{\text{CII}} = 3.47$ , as what was calculated before,  $P_{\text{shot}}^{\text{CII}} = 13.57 \mu\text{K}^2(\text{Mpc}/h)^3$ . We find  $\sigma(f_{\text{NL}}^{\text{loc}}) = 1.32$ , which being of order  $\mathcal{O}(1)$  is the target level of uncertainty needed to discriminate between inflation models. This result deviates from the value of  $\sigma(f_{\text{NL}}^{\text{loc}}) = 1.00$  from Moradinezhad Dizgah & Keating (2019) because we marginalized over an extra parameter  $P_{\text{shot}}^{\text{CII}}$ , and also we adopted an instrumental noise of  $\sim 1220 \mu\text{K}^2\text{-Mpc}^3$ , 22 per cent higher than in Moradinezhad Dizgah & Keating (2019). We plot the  $1-\sigma$  errors in different parameter planes shown as the red ellipses in Fig. 4.

In the second scenario, we include a contamination from one interloper CO( $4 \rightarrow 3$ ) at  $z_j = 0.113$  according to the second term in equation (15), the anisotropic contribution to the [C II] power spectrum due to CO( $4 \rightarrow 3$ ). We focus on this simplified case, since Fig. 1 shows that the power spectrum of CO( $4 \rightarrow 3$ ) is dominant as compared with the other CO lines, especially at large scales where PNG has a bigger effect. The parameter space now includes seven parameters  $\mathbf{q} = \{f_{\text{NL}}^{\text{loc}}, \langle I_{\text{CII}} \rangle, b_{\text{CII}}, \langle I_{\text{CO}(4 \rightarrow 3)}(z_j) \rangle, b_{\text{CO}(4 \rightarrow 3)}(z_j), P_{\text{shot}}^{\text{CII}}, P_{\text{shot}}^{\text{CO}(4 \rightarrow 3)}(z_j)\}$ .

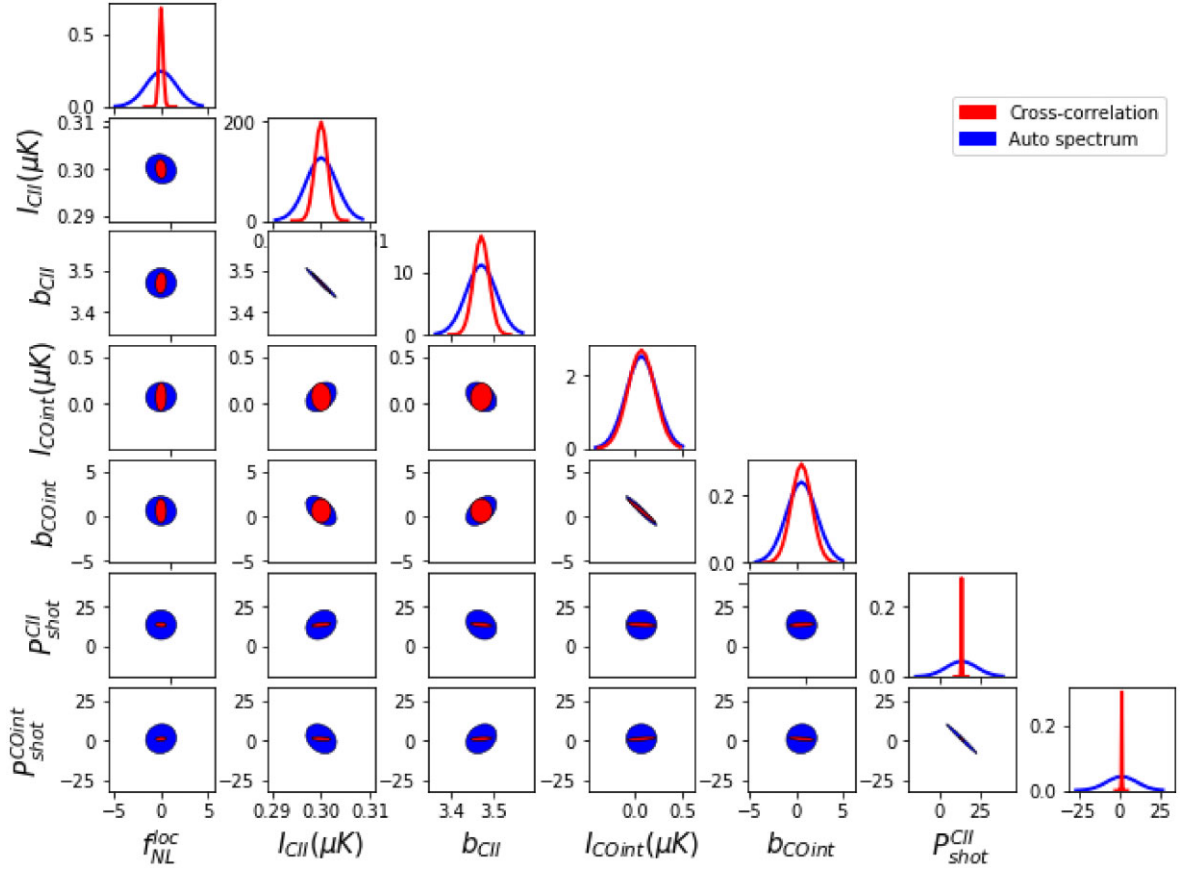


Figure 5.  $1 - \sigma$  forecast of the constraint on  $f_{\text{NL}}^{\text{loc}}$  for the Fisher analysis with considering the CO (4  $\rightarrow$  3) interloper.

We set the fiducial values of the interloper parameters as  $\langle I_{\text{CO}(4 \rightarrow 3)}(z_j) \rangle = 0.07 \text{ } \mu\text{K}$ ,  $b_{\text{CO}(4 \rightarrow 3)}(z_j) = 0.6$  as listed in Table 1,  $P_{\text{shot}}^{\text{CO}(4 \rightarrow 3)}(z_j) = 1.35 \mu\text{K}^2(\text{Mpc}/h)^3$ , and the remaining parameters are set as in the first scenario. We compute the marginalized  $\sigma(f_{\text{NL}}^{\text{loc}}) = 1.64$ , a 24 per cent increase due to interloper contamination. We plot the  $1 - \sigma$  errors in different parameter planes shown as red ellipses in Fig. 5). Alternatively, if we consider the interloper contamination as pure noise other than mixing signals for the target CII line, the parameter space becomes  $\mathbf{q} = \{f_{\text{NL}}^{\text{loc}}, \langle I_{\text{CII}} \rangle, b_{\text{CII}}, P_{\text{shot}}^{\text{CII}}\}$  and we find  $\sigma(f_{\text{NL}}^{\text{loc}}) = 1.60$ . Note that treating the CO(4–3) line as noise gives you slightly less error in  $f_{\text{NL}}^{\text{loc}}$  because this model has less degrees of freedom. The uncertainty in  $f_{\text{NL}}^{\text{loc}}$  becomes much larger when multiple interloper lines are introduced. If we include interloper contamination from all the 7 CO interlopers whose fiducial intensities and biases are given in Table 1 and marginalize over all these fiducial quantities, we get  $\sigma(f_{\text{NL}}^{\text{loc}}) = 4.04$ .

Considering the case where one interloper CO(4  $\rightarrow$  3) biases the measured power spectrum, we get the parameter bias  $\Delta \mathbf{p}^T = [\Delta f_{\text{NL}}^{\text{loc}}, \Delta b_{\text{CII}}, \Delta \langle I_{\text{CII}} \rangle, \Delta P_{\text{shot}}^{\text{CII}}] = [4.54, -5.45, 0.49, 6.87]$ . This would suggest one interloper can masquerade as a  $2.8\sigma$  detection of  $f_{\text{NL}}$ , while providing a false positive for non-standard inflation models. Considering the case where seven CO interlopers bias the measured power spectrum, we get the parameter bias  $\Delta \mathbf{p}^T = [\Delta f_{\text{NL}}^{\text{loc}}, \Delta b_{\text{CII}}, \Delta \langle I_{\text{CII}} \rangle, \Delta P_{\text{shot}}^{\text{CII}}] = [9.21, -10.31, 0.82, 13.51]$ . This would suggest seven interloper can masquerade as a  $2.3\sigma$  detection of  $f_{\text{NL}}$ , while providing a false positive for non-standard inflation models. This result shows that the presence of interlopers are prohibitive when attempting to measure  $f_{\text{NL}}^{\text{loc}}$ , using an autopower spectrum.

## 5 CROSS-CORRELATION WITH OTHER LINES

According to our Fisher analysis results, interloper contamination highly biases local PNG constraints. Next, we consider cross-correlating the target [CII] line with a data cube centred on a different frequency corresponding to a target redshift  $z_t = 3.6$  for the CO (4  $\rightarrow$  3) line, which could reduce the interloper contamination to the PNG constraint. We label the auto power spectra of the [C II] and CO (4  $\rightarrow$  3) at  $z_t = 3.6$  as  $P_{\text{CII}}(k, \mu)$  and  $P_{\text{CO}(4 \rightarrow 3)}(k, \mu)$ , respectively. Assuming C II emitters also emit CO, the upper limit of the cross-power spectrum between the [C II] and CO (4  $\rightarrow$  3) data cubes is

$$P_X(k, \mu) = I_{\text{CII}} I_{\text{CO}(4 \rightarrow 3)} b_{\text{CII}} b_{\text{CO}(4 \rightarrow 3)} (1 + \beta_{\text{CII}} \mu^2) \times (1 + \beta_{\text{CO}(4 \rightarrow 3)} \mu^2) \exp \left( -\frac{k^2 \mu^2 \sigma_v^2}{H^2(z)} \right) P_0(k, z_t) + P_{\text{shot}}^X. \quad (29)$$

The shot noise in the cross-power spectrum is

$$P_{\text{shot}}^X(z) = \frac{c^4 P_{n,\sigma}}{4k_B^2 v_{\text{obsCII}}^2 v_{\text{obsCO}(4 \rightarrow 3)}^2} \int_{M_{\min}}^{M_{\max}} dM \frac{dn}{dM} \times \left[ \frac{L(M, z)}{4\pi \mathcal{D}_L^2} \left( \frac{dl}{d\theta} \right)^2 \frac{dl}{dv} \right]_{\text{CII}} \times \left[ \frac{L(M, z)}{4\pi \mathcal{D}_L^2} \left( \frac{dl}{d\theta} \right)^2 \frac{dl}{dv} \right]_{\text{CO}(4 \rightarrow 3)}. \quad (30)$$

Let the observables be the data vector  $\mathbf{d} = \{P_{\text{C II}}(k, \mu), P_{\text{CO}(4 \rightarrow 3)}(k, \mu), P_x\}$ . We consider a parameter space  $\mathbf{q}$  at  $z_t = 3.6$ . The Fisher matrix element with component for the  $i$ th and  $j$ th of  $\mathbf{q}$  is (Tegmark, Taylor & Heavens 1997)

$$F_{ij} = V_i \int_{-1}^1 d\mu \int_{k_{\min}}^{k_{\max}} \frac{k^2 dk}{8\pi^2} \frac{\partial \mathbf{d}}{\partial q_i} \Xi^{-1} \frac{\partial \mathbf{d}}{\partial q_j} \quad (31)$$

where the entries of the covariance matrix  $\Xi$  are given in Lidz et al. (2009). We can also use equation (20) to compute the shift in the parameters due to interloper contamination. In this case, the formula for  $\Delta D$  becomes

$$\Delta D_j = V_j \int_{-1}^1 d\mu \int_{k_{\min}}^{k_{\max}} \frac{k^2 dk}{8\pi^2} \Delta \mathbf{d} \Xi^{-1} \frac{\partial \mathbf{d}}{\partial q_j}, \quad (32)$$

where  $\Delta \mathbf{d}$  is the shift in the data vector due to interloper contamination.

The Fisher analysis results for this section are listed in Table 2.

We first consider the scenario without interloper lines, i.e. only the first term in equation (15) is considered. The parameter space is  $\mathbf{q} = \{f_{\text{NL}}^{\text{loc}}, \langle I_{\text{C II}}(z_t) \rangle, b_{\text{C II}}(z_t), P_{\text{shot}}^{\text{C II}}(z_t), \langle I_{\text{CO}(4 \rightarrow 3)}(z_t) \rangle, b_{\text{CO}(4 \rightarrow 3)}(z_t), P_{\text{shot}}^{\text{CO}(4 \rightarrow 3)}(z_t), P_x^X\}$ , in which the fiducial values for the  $f_{\text{NL}}^{\text{loc}}$ ,  $\langle I_{\text{C II}}(z_t) \rangle$ ,  $b_{\text{C II}}(z_t)$  are set as in Section 4,  $\langle I_{\text{CO}(4 \rightarrow 3)}(z_t) \rangle$  and  $b_{\text{CO}(4 \rightarrow 3)}(z_t)$  are calculated from the method discussed in Section 2,  $\langle I_{\text{CO}(4 \rightarrow 3)}(z_t) \rangle = 0.60 \mu\text{K}$ ,  $b_{\text{CO}(4 \rightarrow 3)}(z_t) = 2.8$ ,  $P_{\text{shot}}^{\text{CO}(4 \rightarrow 3)}(z_t) = 88.01 \mu\text{K}^2 (\text{Mpc}/h)^3$ ,  $P_x^X = 32.13 \mu\text{K}^2 (\text{Mpc}/h)^3$ . We use the  $8 \times 8$  Fisher matrix from equation (31) to find the constraint on the parameters.  $1 - \sigma$  errors in different parameter planes are shown as the red ellipses in Fig. 4. In this Fisher analysis assuming the data set  $\{P_{\text{C II}}(k, \mu), P_{\text{CO}(4 \rightarrow 3)}(k, \mu), P_x\}$ , we find  $\sigma(f_{\text{NL}}^{\text{loc}}) = 0.65$ , much lower than the initial experimental set-up value for the [C II] autopower spectrum of  $\sigma(f_{\text{NL}}^{\text{loc}}) = 1.32$ . This result is expected since having multiple lines add more constraining power, and we benefit from the multitracers cosmic variance cancellation, as addressed in Liu & Breysse (2021).

In the second scenario, we include the contamination from one interloper CO(4  $\rightarrow$  3) at redshift 0.113 according to the second term in equation (15), the anisotropic contribution to the [C II] power spectrum due to CO(4  $\rightarrow$  3). The parameter space includes eleven parameters  $\mathbf{q} = \{f_{\text{NL}}^{\text{loc}}, \langle I_{\text{C II}}(z_t) \rangle, b_{\text{C II}}(z_t), P_{\text{shot}}^{\text{C II}}(z_t), \langle I_{\text{CO}(4 \rightarrow 3)}(z_t) \rangle, b_{\text{CO}(4 \rightarrow 3)}(z_t), P_{\text{shot}}^{\text{CO}(4 \rightarrow 3)}(z_t), \langle I_{\text{int CO}(4 \rightarrow 3)}(z_j) \rangle, b_{\text{int CO}(4 \rightarrow 3)}(z_j), P_{\text{shot}}^{\text{int CO}(4 \rightarrow 3)}(z_j), P_x^X\}$ , in which the fiducial values  $\langle I_{\text{int CO}(4 \rightarrow 3)}(z_j) \rangle$  and  $b_{\text{int CO}(4 \rightarrow 3)}(z_j)$  for the interloper parameters are set as Section 4.2. We use the  $11 \times 11$  Fisher matrix from equation (31) to find the constraint on the parameters.  $1 - \sigma$  errors in different parameter planes are shown as the red ellipses in Fig. 5. We find that in this Fisher analysis  $\sigma(f_{\text{NL}}^{\text{loc}}) = 0.69$ , which is only 6 per cent more than the predicted  $f_{\text{NL}}$  error in the case with no interlopers. Note this increase is 4x less than the increase in the  $f_{\text{NL}}$  error from the autopower spectrum constraint. We also see that the error for the two cross-correlation cases, one with no interlopers and one with interlopers, are equal within less than 6 per cent, suggesting that interlopers do not significantly bias measurements of  $f_{\text{NL}}$  when the auto and cross-power spectra are used jointly. Alternatively, if we consider the interloper contamination as pure noise other than mixing signals for the target C II line, we find  $\sigma(f_{\text{NL}}^{\text{loc}}) = 0.78$ , the parameter bias  $\Delta \mathbf{p}^T = \Delta[f_{\text{NL}}^{\text{loc}}, \langle I_{\text{C II}}(z_t) \rangle, b_{\text{C II}}(z_t), \langle I_{\text{CO}(4 \rightarrow 3)}(z_t) \rangle, b_{\text{CO}(4 \rightarrow 3)}(z_t), P_{\text{shot}}^{\text{C II}}(z_t), P_{\text{shot}}^{\text{CO}(4 \rightarrow 3)}(z_t)] = [3.29, 0.21, -2.29, -0.037, 0.15, 6.77, 30.89]$ . This results shows that including the interlopers as pure noise other than signals cannot help to remove the interloper contamination. If we assume the data set only includes the cross-spectrum  $\{P_x\}$ , we find  $\sigma(f_{\text{NL}}^{\text{loc}}) = 0.85$ , slightly higher than that from doing the

**Table 3.** Fisher analysis results for  $f_{\text{NL}}^{\text{orth}}$ .

Interloper number	0	1
$\sigma(f_{\text{NL}}^{\text{orth}})$ for autospectrum	52.75	7.15
$\sigma(f_{\text{NL}}^{\text{orth}})$ for cross-correlation	42.24	7.05

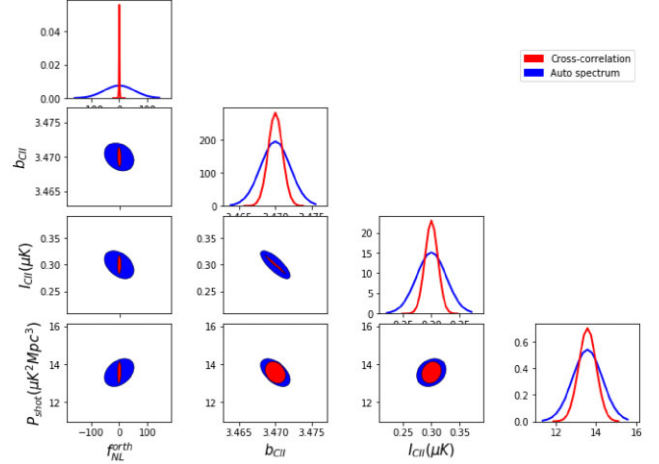


**Figure 6.**  $1 - \sigma$  forecast of the constraint on  $f_{\text{NL}}^{\text{orth}}$  for the Fisher analysis without considering interlopers.

cross-correlation considering autospectrum. This result shows that including the autospectrum reduces the error by less than 10 per cent if you treat the interlopers as noise.

If we include all the seven interlopers CO(4  $\rightarrow$  3) to CO(10  $\rightarrow$  9) at lower redshift, with all their intensities and biases being added to the parameter space  $\mathbf{q}$ , in the cross-correlated Fisher analysis we get  $\sigma(f_{\text{NL}}^{\text{loc}}) = 0.85$ , dropping significantly as compared to  $\sigma(f_{\text{NL}}^{\text{loc}}) = 4.04$  for the [C II] autopower spectrum Fisher analysis.

## 6 CONSTRAINTS ON ORTHOGONAL SHAPE PNG

In this section, we derive how interlopers affect constraints on measurements of orthogonal shape PNG. We present the forecasts for the removal of CO interloper contributions to the [C II] autopower spectrum detection in the first subsection. In the second subsection, we present the Fisher forecasts for the cross-correlation between [C II] line and other lines at the same redshift. The Fisher analysis results for this section are listed in Table 3.

### 6.1 Autopower spectrum Fisher forecast

We forecast the orthogonal shape PNG rather than the equilateral PNG since the former brings larger correction to the clustering bias, and thus a stronger constraint on  $f_{\text{NL}}$ . We set the fiducial value  $f_{\text{NL}}^{\text{orth}} = 0$ . We adopt the same fiducial survey and remaining parameter values as described in Section 4.

In the first scenario we assume there is no interloper contamination. The parameter space includes four parameters  $\mathbf{q} = \{f_{\text{NL}}^{\text{orth}}, \langle I_{\text{C II}} \rangle, b_{\text{C II}}, P_{\text{shot}}^{\text{C II}}\}$ . We find  $\sigma(f_{\text{NL}}^{\text{orth}}) = 52.75$ , and we plot the  $1 - \sigma$  errors in different parameter planes shown as red ellipses in Fig. 6.

In the second scenario, we include the interloper contamination from one interloper CO(4  $\rightarrow$  3) at  $z_j = 0.113$ . The parameter space contains seven parameters  $\mathbf{q} =$



$\{f_{\text{NL}}^{\text{orth}}, \langle I_{\text{CII}}(z_t) \rangle, b_{\text{CII}}(z_t), P_{\text{shot}}^{\text{CII}}(z_t), \langle I_{\text{CO}(4 \rightarrow 3)}(z_j) \rangle, b_{\text{CO}(4 \rightarrow 3)}(z_j), P_{\text{shot}}^{\text{CO}(4 \rightarrow 3)}(z_j)\}$ . We plot the  $1 - \sigma$  errors in different parameter planes shown as red ellipses in Fig. 7. We find the marginalized  $\sigma(f_{\text{NL}}^{\text{orth}}) = 42.24$ . The reason for this error being smaller than that in the first scenario, as contrary to the case for  $f_{\text{NL}}^{\text{loc}}$  is that  $\Delta b_h^{\text{orth}}$  in equation (4) are of the same sign for the target line and the interloper, while  $\Delta b_h^{\text{loc}}$  in equation (3) are of different signs.

Considering the case where one interloper  $P_{\text{CO}(4 \rightarrow 3)}$  biases the measured power spectrum, we compute the parameter bias  $\Delta \mathbf{p}^T = [\Delta f_{\text{NL}}^{\text{orth}}, \Delta b_{\text{CII}}, \Delta \langle I_{\text{CII}} \rangle, \Delta P_{\text{shot}}^{\text{CII}}] = [49.20, -5.58, 0.51, 6.25]$ . This points to a modest bias relative to the predicted errors, in that the interlopers could masquerade as a  $1.2\sigma$  measurement of  $f_{\text{NL}}$ .

## 6.2 Cross-correlation Fisher forecast

We adopt the same fiducial survey and value of parameters for cross-correlation as in Section 5. We first consider the scenario without interloper lines with the parameter space being  $\mathbf{q} = \{f_{\text{NL}}^{\text{orth}}, \langle I_{\text{CII}}(z_t) \rangle, b_{\text{CII}}(z_t), P_{\text{shot}}^{\text{CII}}(z_t), \langle I_{\text{CO}(4 \rightarrow 3)}(z_j) \rangle, b_{\text{CO}(4 \rightarrow 3)}(z_j), P_{\text{shot}}^{\text{CO}(4 \rightarrow 3)}(z_j), P_{\text{shot}}^{\text{X}}(z_j)\}$ .  $1 - \sigma$  errors in different parameter planes are shown as red ellipses in Fig. 6. We find that in this cross-correlated Fisher analysis  $\sigma(f_{\text{NL}}^{\text{orth}}) = 7.05$ , dropping significantly as compared to  $\sigma(f_{\text{NL}}^{\text{orth}}) = 52.75$  for the [CII] auto power spectrum Fisher analysis.

In the second scenario we include the interloper contamination from one interloper CO (4 → 3) at redshift 0.113. The parameter space includes seven parameters  $\mathbf{q} = \{f_{\text{NL}}^{\text{orth}}, \langle I_{\text{CII}}(z_t) \rangle, b_{\text{CII}}(z_t), P_{\text{shot}}^{\text{CII}}(z_t), \langle I_{\text{CO}(4 \rightarrow 3)}(z_j) \rangle, b_{\text{CO}(4 \rightarrow 3)}(z_j), P_{\text{shot}}^{\text{CO}(4 \rightarrow 3)}(z_j), \langle I_{\text{int CO}(4 \rightarrow 3)}(z_j) \rangle, b_{\text{int CO}(4 \rightarrow 3)}(z_j), P_{\text{shot}}^{\text{CO}(4 \rightarrow 3)}(z_j), P_{\text{shot}}^{\text{X}}(z_j)\}$ .  $1 - \sigma$  errors in different parameter planes are shown as red ellipses in Fig. 7. We note that in this cross-correlated Fisher analysis  $\sigma(f_{\text{NL}}^{\text{orth}}) = 7.05$ , dropping significantly as compared to  $\sigma(f_{\text{NL}}^{\text{orth}}) = 42.24$  for the [CII] auto power spectrum Fisher analysis. Similar to the local PNG case, cross-power spectra tend to remove the effect of interlopers when measuring  $f_{\text{NL}}$ . Alternatively, if we consider the interloper contamination as pure noise other than mixing signals for the target CII line, we find  $\sigma(f_{\text{NL}}^{\text{orth}}) = 7.29$ , the parameter bias  $\Delta \mathbf{p}^T = [f_{\text{NL}}^{\text{orth}}, \langle I_{\text{CII}}(z_t) \rangle, b_{\text{CII}}(z_t), \langle I_{\text{CO}(4 \rightarrow 3)}(z_t) \rangle, b_{\text{CO}(4 \rightarrow 3)}(z_t), P_{\text{shot}}^{\text{CII}}(z_t), P_{\text{shot}}^{\text{CO}(4 \rightarrow 3)}(z_t)] = [59.31, 0.47, -5.53, 0.041, -0.20, 6.56, 30.84]$ . This result shows that including the interlopers as pure noise other than signals cannot help to remove the interloper contamination. If we assume the data set only includes the cross-spectrum  $\{P_x\}$ , we find  $\sigma(f_{\text{NL}}^{\text{orth}}) = 13.51$ , larger than that from considering both the cross-spectrum and the autospectra. This result shows that including the autospectrum is necessary for removing the interlopers when treating it as noise.

## 7 DISCUSSION

In this section, we discuss how the PNG constraints depend on astrophysical models. Specifically, we consider how both different modelling of CO line luminosity and the minimum mass of haloes that emit lines affect the PNG constraints.

We set  $M_{\text{min}} = 10^9 M_{\odot}$  in our base model. In the fiducial [C II] model we use throughout the paper, we set the minimum halo mass for [C II] line emission to be  $M_{\text{min}} = 10^9 M_{\odot}$ . This parameter is very uncertain, with reasonable values between  $M_{\text{min}} = 10^9 - 10^{11} M_{\odot}$ . We find when setting  $M_{\text{min}} = 10^{10} M_{\odot}$  without considering interloper contamination,  $\langle I_{\text{CII}}(z_t) \rangle$  gets lower and therefore yields

a weaker constraint. Specifically, for the case with only the autopower spectrum only and no interlopers present,  $\sigma(f_{\text{NL}}^{\text{loc}}) = 1.54$ , a 17 per cent increase from 1.32, the error for autospectrum case for no interlopers when  $M_{\text{min}} = 10^9 M_{\odot}$ . For the case with both autopower and cross-power spectrum and no interlopers present,  $\sigma(f_{\text{NL}}^{\text{loc}}) = 0.78$ , a 13 per cent increase from 0.65, the error for both autospectrum and cross-power spectrum case for no interlopers when  $M_{\text{min}} = 10^9 M_{\odot}$ . For the case with only the autopower spectrum only and one interlopers present,  $\sigma(f_{\text{NL}}^{\text{loc}}) = 1.95$ , a 19 per cent increase from 1.64, the error for autospectrum case for one interlopers when  $M_{\text{min}} = 10^9 M_{\odot}$ . For the case with both autopower and cross-power spectrum and one interlopers present,  $\sigma(f_{\text{NL}}^{\text{loc}}) = 0.82$ , a 19 per cent increase from 0.69, the error for both autospectrum and cross-power spectrum case for one interlopers when  $M_{\text{min}} = 10^9 M_{\odot}$ .

For the fiducial CO model in this work we use the Li et al. (2016) model for the interlopers. Including only one CO interloper CO(4 → 3) line contamination, we consider two other models with the CO luminosity linearly related to the halo mass. In model considering  $f_{\text{duty}} = t_s/t_{\text{age}}(z)$  in Pullen et al. (2013), we find a lower intensity for CO(4 → 3), and thus a stronger constraint on PNG. Specifically, for the autopower only case with one interloper we find  $\sigma(f_{\text{NL}}^{\text{loc}}) = 1.55$ , a 5 per cent reduction from 1.64, the error for autospectrum case for one interlopers; for the case with both autopower and cross-power,  $\sigma(f_{\text{NL}}^{\text{loc}}) = 0.67$ , a 3 per cent reduction from 0.69, the error for autospectrum case for one interlopers. In Keating et al. (2016), we get higher intensity for CO(4 → 3), and thus a weaker constraint on PNG with  $\sigma(f_{\text{NL}}^{\text{loc}}) = 1.76$  and  $\sigma(f_{\text{NL}}^{\text{loc}}) = 0.83$  for cases with only autopower and with both autopower and cross-power spectrum, respectively.

We use the luminosity model in Visbal & Loeb (2010) to get the intensity ratios between CO( $J \rightarrow J - 1$ ) and CO(1 → 0). Considering instead the relationship CO( $J \rightarrow J - 1$ ) =  $\beta^3$  CO(1 → 0) in Obreschkow et al. (2009) and get higher interloper intensities, and thus a weaker constraint on PNG with  $\sigma(f_{\text{NL}}^{\text{loc}}) = 4.80$  if we include seven interlopers. While the relationship of CO( $J \rightarrow J - 1$ ) = CO(1 → 0) in Lidz et al. (2011) yields lower interloper intensities, and thus a stronger constraint on PNG with  $\sigma(f_{\text{NL}}^{\text{loc}}) = 1.34$  and  $\sigma(f_{\text{NL}}^{\text{loc}}) = 0.60$  for cases with only autopower and with both autopower and cross-power spectrum, respectively.

We set  $k_{\parallel, \text{min}} = 0.0077 \text{ Mpc}^{-1}$  in our base model. To model the effect of more severe cuts due to continuum foreground contamination, we consider a higher  $k_{\parallel, \text{min}}$ . Specifically, if we set  $k_{\parallel, \text{min}} = 0.077$ , for the case with only the autopower spectrum only and no interlopers present,  $\sigma(f_{\text{NL}}^{\text{loc}}) = 1.50$ , a 14 per cent increase from 1.32, the error for autospectrum case for no interlopers when  $k_{\parallel, \text{min}} = 0.0077 \text{ Mpc}^{-1}$ . The increase in error was relatively small because these scales were already down-weighted in the base forecast. For the case with both autopower and cross-power spectrum and no interlopers present  $\sigma(f_{\text{NL}}^{\text{loc}}) = 0.86$ , a 11 per cent increase from 0.65, the error for both autospectrum and cross-power spectrum case for no interlopers when  $k_{\parallel, \text{min}} = 0.0077 \text{ Mpc}^{-1}$ . For the case with only the autopower spectrum only and one interlopers present,  $\sigma(f_{\text{NL}}^{\text{loc}}) = 1.87$ , a 15 per cent increase from 1.64, the error for autospectrum case for one interlopers when  $k_{\parallel, \text{min}} = 0.0077 \text{ Mpc}^{-1}$ . For the case with both autopower and cross-power spectrum and one interlopers present,  $\sigma(f_{\text{NL}}^{\text{loc}}) = 0.80$ , a 16 per cent increase from 0.69, the error for both autospectrum and cross-power spectrum case for one interlopers when  $k_{\parallel, \text{min}} = 0.0077 \text{ Mpc}^{-1}$ . Note that the relative increases in error due to interloper contamination do not change significantly due to having a higher  $k_{\parallel, \text{min}}$  cut.



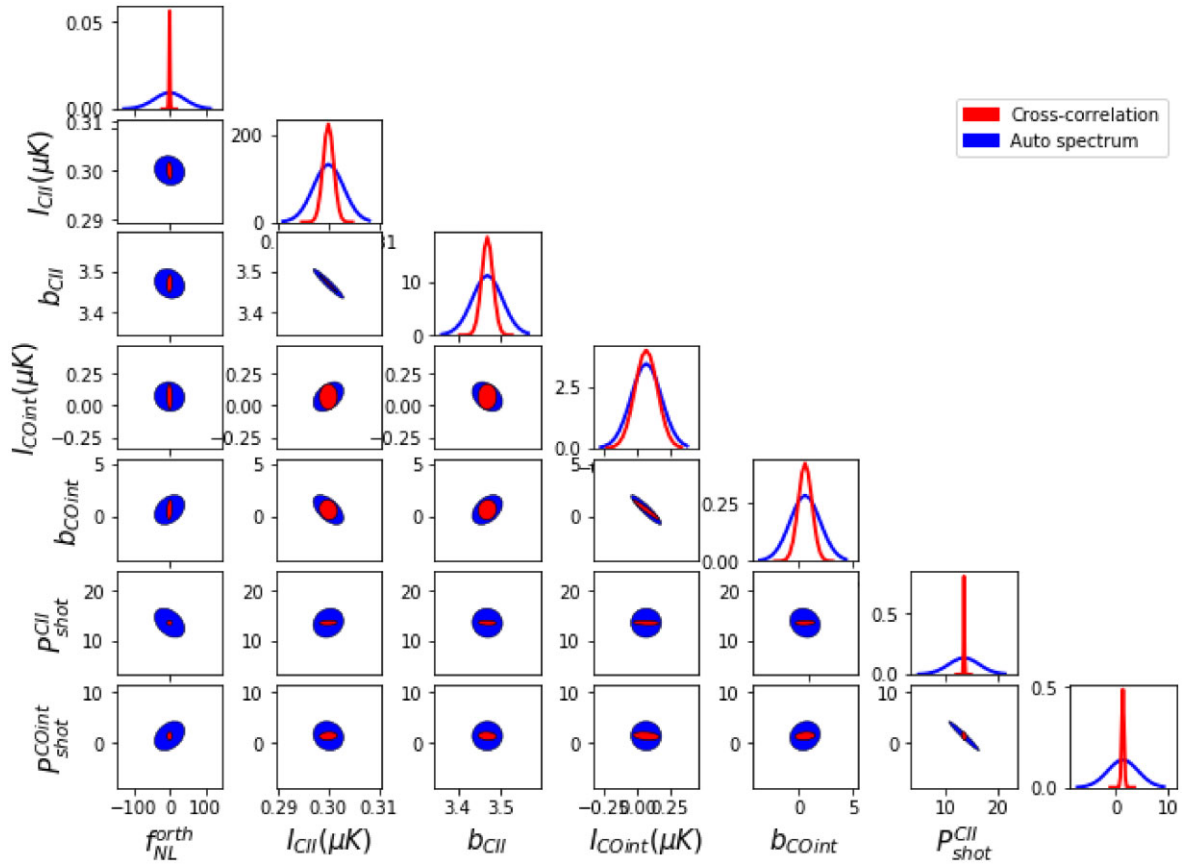


**Figure 7.**  $1 - \sigma$  forecast of the constraint on  $f_{\text{NL}}^{\text{orth}}$  for the Fisher analysis with considering CO (4  $\rightarrow$  3) interloper.

We set  $\theta_{\text{max}} = 118^\circ$  in our base model. If the sky coverage is as small as  $\theta_{\text{max}} = 59^\circ$ , the survey volume is quartered and  $k_{\perp, \text{min}}$  increases. Specifically, for the case with only the autopower spectrum and no interlopers present,  $\sigma(f_{\text{NL}}^{\text{loc}}) = 2.40$ , an 82 per cent increase from 1.32, the error for autospectrum case for no interlopers when  $\theta_{\text{max}} = 118^\circ$ . For the case with both autopower and cross-power spectrum and no interlopers present  $\sigma(f_{\text{NL}}^{\text{loc}}) = 1.24$ , a 91 per cent increase from 0.65, the error for both autospectrum and cross-power spectrum case for no interlopers when  $\theta_{\text{max}} = 118^\circ$ . For the case with only the autopower spectrum only and one interlopers present,  $\sigma(f_{\text{NL}}^{\text{loc}}) = 3.02$ , a 84 per cent increase from 1.64, the error for autospectrum case for one interlopers when  $\theta_{\text{max}} = 118^\circ$ . For the case with both autopower and cross-power spectrum and one interlopers present,  $\sigma(f_{\text{NL}}^{\text{loc}}) = 1.26$ , a 82 per cent increase from 0.69, the error for both autospectrum and cross-power spectrum case for one interlopers when  $\theta_{\text{max}} = 118^\circ$ . Note that the relative increases in error due to interloper contamination do not change significantly due to having less survey area.

If we half the value of the instrumental noise, for the case with only the autopower spectrum only and no interlopers present,  $\sigma(f_{\text{NL}}^{\text{loc}}) = 1.14$ , a 14 per cent decrease from 1.32, the error for autospectrum case for no interlopers. For the case with both autopower and cross-power spectrum and no interlopers present  $\sigma(f_{\text{NL}}^{\text{loc}}) = 0.54$ , a 17 per cent decrease from 0.65, the error for both autospectrum and cross-power spectrum case for no interlopers. For the case with only the autopower spectrum only and one interlopers present,  $\sigma(f_{\text{NL}}^{\text{loc}}) = 1.27$ , a 23 per cent decrease from 1.64, the error for autospectrum case for one interlopers. For the case with both

autopower and cross-power spectrum and one interlopers present,  $\sigma(f_{\text{NL}}^{\text{loc}}) = 0.59$ , a 15 per cent decrease from 0.69, the error for both autospectrum, and cross-power spectrum case for one interlopers.

## 8 CONCLUSION

Probing constraints on PNG characterized by  $f_{\text{NL}}$  is a strong discriminant among cosmological models. PNG leads to a scale-dependent clustering bias for emission lines. We consider [C II] LIM at the target redshift  $z_t = 3.6$  to model how interlopers affect measurements of  $f_{\text{NL}}^{\text{loc}}$  and  $f_{\text{NL}}^{\text{orth}}$ .

Interloper contamination from CO line confusion provides an important systematic concern for our intensity mapping method. We separate the anisotropic CO interloper contamination at the power spectrum level. We obtained constraints on  $f_{\text{NL}}$  from a future survey with and without CO lines interloping, and found that the interloper contamination leads to weaker constraints on  $f_{\text{NL}}$  along with significant bias to the parameter.

We model the cross-correlation between [C II] and CO(4–3) at the same redshift as a way to reduce the interloper contamination at target redshift. We model constraints on  $f_{\text{NL}}$  by calculating auto power spectrum and cross power spectrum between the data cubes which contain [C II] and CO(4–3). We find the interloper contamination for the PNG probing can be largely removed using this method.

PNG will shed light on physics of primordial fluctuations. LIM is a potential technique to probe PNG by providing complimentary information undetectable with other traditional galaxy surveys. Interloper contamination is an important systematic concern for this

technique, as obtained by using the power anisotropy separation method, but it can be reduced largely by using cross-correlation techniques.

## ACKNOWLEDGEMENTS

We thank Patrick Breyse for his helpful feedback on an earlier version of this manuscript. ARP was supported by the Simons Foundation and by NASA under award numbers 80NSSC18K1014 and NNH17ZDA001N.

## DATA AVAILABILITY

The data used to support the findings of this study are available from the corresponding author upon request.

## REFERENCES

- Abbott T. M. C. et al., 2018, *Phys. Rev. D*, 98, 043526  
 Afshordi N., Tolley A. J., 2008, *Phys. Rev. D*, 78, 123507  
 Alam S. et al., 2017, *MNRAS*, 470, 2617  
 Amendola L. et al., 2018, *Living Rev. Rel.*, 21, 2  
 Behroozi P. S., Wechsler R. H., Conroy C., 2013, *ApJ*, 762, L31  
 Carilli C. L., Walter F., 2013, *ARA&A*, 51, 105  
 Castorina E. et al., 2019, *J. Cosmol. Astropart. Phys.*, 2019, 010  
 Cheng Y.-T., Chang T.-C., Bock J., Bradford C. M., Cooray A., 2016, *ApJ*, 832, 165  
 Dai J.-P., Xia J.-Q., 2020, *MNRAS*, 491, L61  
 Dalal N., Doré O., Huterer D., Shirokov A., 2008, *Phys. Rev. D*, 77, 123514  
 Desjacques V., Jeong D., Schmidt F., 2011, *Phys. Rev. D*, 84, 063512  
 Gangui A., Lucchin F., Matarrese S., Mollerach S., 1994, *ApJ*, 430, 447  
 Gong Y., Cooray A., Silva M., Santos M. G., Bock J., Bradford C. M., Zemcov M., 2012, *ApJ*, 745, 49  
 Gong Y., Silva M., Cooray A., Santos M. G., 2014, *ApJ*, 785, 72  
 Gong Y., Chen X., Cooray A., 2020, *ApJ*, 894, 152  
 Guth A. H., 1981, *Phys. Rev. D*, 23, 347  
 Ho S. et al., 2015, *J. Cosmol. Astropart. Phys.*, 2015, 040  
 Jackson J. C., 1972, *MNRAS*, 156, 1P  
 Kaiser N., 1987, *MNRAS*, 227, 1  
 Keating G. K., Marrone D. P., Bower G. C., Leitch E., Carlstrom J. E., DeBoer D. R., 2016, *ApJ*, 830, 34

- Kennicutt Robert C. J., 1998, *ARA&A*, 36, 189  
 Komatsu E., Spergel D. N., 2001, *Phys. Rev. D*, 63, 063002  
 Kovetz E. et al., 2019, *BAAS*, 51, 101  
 Leistedt B., Peiris H. V., Roth N., 2014, *Phys. Rev. Lett.*, 113, 221301  
 Li T. Y., Wechsler R. H., Devaraj K., Church S. E., 2016, *ApJ*, 817, 169  
 Lidz A., Taylor J., 2016, *ApJ*, 825, 143  
 Lidz A., Zahn O., Furlanetto S. R., McQuinn M., Hernquist L., Zaldarriaga M., 2009, *ApJ*, 690, 252  
 Lidz A., Furlanetto S. R., Oh S. P., Aguirre J., Chang T.-C., Doré O., Pritchard J. R., 2011, *ApJ*, 741, 70  
 Linde A. D., 1987, A New Inflationary Universe Scenario: A Possible Solution of the Horizon, Flatness, Homogeneity, Isotropy and Primordial Monopole Problems. World Scientific, Singapore, p. 149  
 Linde A., Mukhanov V., 1997, *Phys. Rev. D*, 56, R535  
 Liu R. H., Breyse P. C., 2021, *Phys. Rev. D*, 103, 063520  
 Lyth D. H., Ungarelli C., Wands D., 2003, *Phys. Rev. D*, 67, 023503  
 Maldacena J., 2003, *J. High Energy Phys.*, 2003, 013  
 Matarrese S., Verde L., 2008, *ApJ*, 677, L77  
 Moradinezhad Dizgah A., Keating G. K., 2019, *ApJ*, 872, 126  
 Moradinezhad Dizgah A., Keating G. K., Fialkov A., 2019, *ApJ*, 870, L4  
 Obreschkow D., Heywood I., Klöckner H. R., Rawlings S., 2009, *ApJ*, 702, 1321  
 Planck Collaboration IX, 2019, *A&A*, 641, A9  
 Pullen A. R., Chang T.-C., Doré O., Lidz A., 2013, *ApJ*, 768, 15  
 Pullen A. R., Hirata C. M., Doré O., Raccanelli A., 2016, *PASJ*, 68, 12  
 Robertson B. E., Ellis R. S., Furlanetto S. R., Dunlop J. S., 2015, *ApJ*, 802, L19  
 Senatore L., Smith K. M., Zaldarriaga M., 2010, *J. Cosmol. Astropart. Phys.*, 2010, 028  
 Silva M., Santos M. G., Cooray A., Gong Y., 2015, *ApJ*, 806, 209  
 Slosar A., Hirata C., Seljak U., Ho S., Padmanabhan N., 2008, *J. Cosmol. Astropart. Phys.*, 2008, 031  
 Tegmark M., Taylor A., Heavens A., 1997, *Astrophys. J.*, 480, 22  
 Tinker J., Kravtsov A. V., Klypin A., Abazajian K., Warren M., Yepes G., Gottlöber S., Holz D. E., 2008, *ApJ*, 688, 709  
 Tinker J. L., Robertson B. E., Kravtsov A. V., Klypin A., Warren M. S., Yepes G., Gottlöber S., 2010, *ApJ*, 724, 878  
 Visbal E., Loeb A., 2010, *J. Cosmol. Astropart. Phys.*, 2010, 016

This paper has been typeset from a  $\text{\LaTeX}$  file prepared by the author.